Chapter 5

Impinging Jet Flow

5.1 Introduction

The axisymmetric impinging jet flow is geometrically simple. Figure 5.1 shows a schematic of the particular arrangement considered in the current work. The fully-developed pipe flow exits the pipe of diameter D at a height of 4 jet diameters from the wall $(H/D = 4)$, impinges onto the wall surface and spreads radially outwards. Figure 5.2 shows a typical velocity vector plot. The Reynolds number of the flow, based on the bulk inlet velocity and pipe diameter, is $Re = 70,000$ and conditions were chosen to match the experimental measurements of Baughn *et al*. [94] and Cooper *et al*. [95].

There have been numerous computational and experimental studies of the impinging jet and this reflects the range of related industrial flows and the usefulness of this particular geometry for testing turbulence models. Jet impingement causes high levels of heat-transfer coefficient near the stagnation point and is used in industrial applications where heating, cooling or drying processes are required. Flow impingement occurs on the upstream face of bluff bodies, such as the simplified car body examined in Chapter 7. As a test case, the impinging jet offers insight into the behaviour of turbulence models in flow regimes far removed from the traditional simple shear flow. In an axisymmetric im-

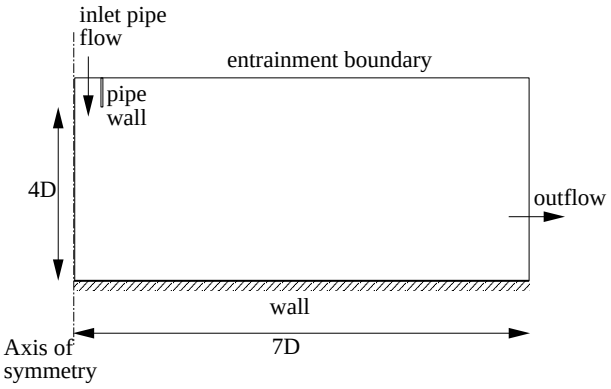

Figure 5.1: Impinging jet flow domain and boundary conditions.

pinging jet, there is significant irrotational straining near the stagnation point and, near the edge of the impinging jet, there is strong streamline curvature. Moving further downstream, the flow tends towards a simple radial wall jet, but one in which the maximum shear stress occurs outside the wall region [95].

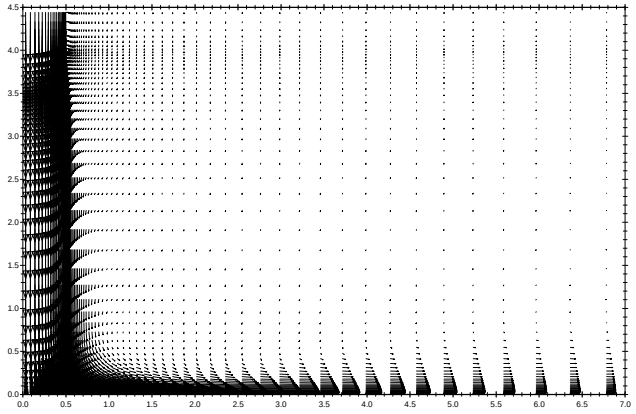

Figure 5.2: Predicted velocity vectors for the impinging jet flow ($Re = 70,000$, $H/D = 4$) using the Craft *et al*. NLEVM

For the purposes of examining the processes involved in the impinging jet flow, the flow domain can be decomposed into three regions. These regions are identified on the plot of experimental Nusselt number[1] shown in Figure 5.3. In the first region, on the axis of symmetry ($r/D = 0$, where r is the radial distance from the axis of symmetry) the mean shear strain is zero and turbulence energy production is from normal straining. The heat transfer rate is greatest at the stagnation point, with Nu at its maximum. Since the jet considered in the current calculations is only four diameters away from the wall, there is insufficient height for significant mixing to occur with the surrounding fluid between the jet inlet and the wall. Therefore the fluid convected into the near-wall region has a low turbulence intensity (similar to that in the fully developed pipe flow) and is at a temperature close to the inlet condition. The thermal boundary layer is confined to the width of the viscous sublayer which is itself thin at this point. In the region between the axis of symmetry and $r/D \approx 1$, the RMS fluctuating velocity component in the wall-normal direction $\left(v^{'}\right)$ exceeds that parallel to the wall $\left(u^{'}\right)$ in contrast to fully-developed channel flows where the $u^{'}$ component is greater than $v^{'}$ (see Figure 1.2). The turbulence length scale $(k^{3/2}/\varepsilon)$ near the wall is strongly affected by length scales of the jet turbulence, retaining a memory of upstream history, whereas in simple shear flows the length scale is a function only of the wall distance. Convective transport of turbulence energy towards the stagnation point is also important (i.e. the flow is not in local equilibrium). The Nusselt number steadily drops

[1]The Nusselt number is a dimensionless heat transfer coefficient proportional to the ratio of the heat transfer by convection to the heat transfer by conduction, which in the impinging jet flow is evaluated as:

$$Nu = \frac{hD}{\lambda} = \frac{q_{wall} D\sigma}{\mu c_p \left(T_{wall} - T_{in}\right)} \tag{5.1}$$

where D is the jet diameter and T_{in} the inlet temperature.

from its maximum at the stagnation point towards a minimum at $r/D \approx 1$. In this region, strong flow curvature has a stabilizing effect on the flow, reducing turbulence energy[2]. In the second region, further downstream $(1 < r/D < 2)$, the Nusselt number rises up to a secondary peak. Here, there is significant acceleration of the fluid away from the stagnation point which in itself might be expected to cause a reduction in turbulence levels. However, as one moves away from the stagnation point (where turbulence levels are low) high near-wall shear strains develop which generate turbulence energy. In addition, the mixing layer around the edge of the jet reaches the wall in this region, bringing with it higher levels of turbulence energy. The fluctuating velocity parallel to the wall also shows an increase relative to the normal component between $r/D = 1$ and 2 (Figure 5.13). In the radial-wall-jet region $(r/D > 2)$, the Nusselt number decreases at a gradually decreasing rate as the thickness of the viscous and thermal boundary layers increase and the radial velocity falls as the wall jet spreads. The near-wall kinetic energy steadily decreases although the maximum turbulent stress levels are more than twice as high as in the corresponding plane wall jet [65, 95].

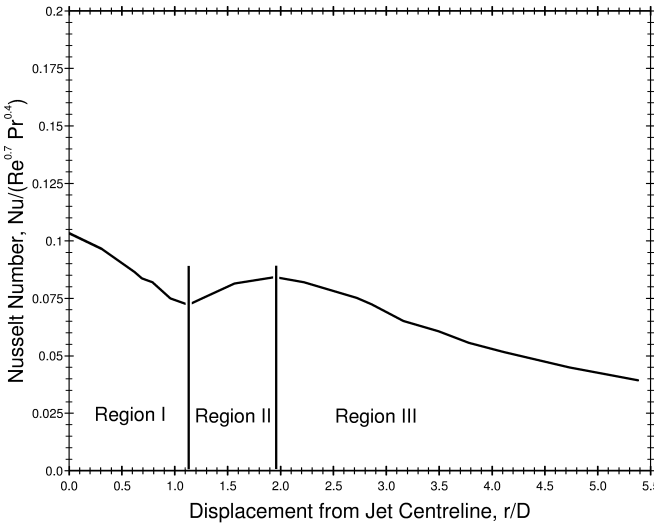

Figure 5.3: Experimental Nusselt number data for the impinging jet ($Re = 70,000$ and $H/D = 4$) from Baughn *et al*. [94] showing the three main flow regions.

5.2 Previous Experimental and Computational Studies

It is well known that the low-*Re* linear $k-\varepsilon$ model overpredicts the level of turbulent kinetic energy at the stagnation point in impinging flows. The Yap correction [64] and the more recent differential

[2]If one considers the kinetic energy production due to shear stress in this region (in 2-*D* Cartesian coordinates), the production of k due to shear stress, $P_{kuv} = -\rho\overline{uv}(\partial U/\partial y + \partial V/\partial x)$, where the shear strain rates $\partial U/\partial y$ and $\partial V/\partial x$ are of opposite sign, tending to reduce P_k and hence k. Normal strain rates $\partial U/\partial x$ and $\partial V/\partial y$ are also of opposite sign and hence kinetic energy production due to normal stresses $\overline{u^2}$ and $\overline{v^2}$ are of the opposite sign, further diminishing P_k (see Bradshaw [96]).

length-scale correction of Iacovides & Raisee [66, 67] improve this behaviour somewhat, although heat transfer rates at the stagnation point are still overpredicted by a factor of nearly two (see results below). An explanation for the behaviour of the linear $k-\varepsilon$ model was provided by Kato & Launder [97] who showed that using this model the production rate of kinetic energy can be written as:

$$P_k = -\rho\overline{u_i u_j}\frac{\partial U_i}{\partial x_j} = \rho c_\mu \varepsilon S^2 \tag{5.2}$$

Near the stagnation point, the irrotational strain field leads to a high value of the dimensionless strain invariant, S, which in turn leads to a large P_k. Kato & Launder suggested a modified production term in which S^2 is replaced with ΩS. Since the vorticity invariant, Ω, is small in irrotational straining, the production term takes a more realistic value. Although the Kato-Launder modification improves the $k-\varepsilon$ model predictions in impinging flows, it was suggested that their correction should not be considered a permanent fix since it would lead to an overly large production in rotating and swirling flows. An alternative remedy of the stagnation-point problem by Durbin [98] imposed a limit on the turbulence time-scale $(T = k/\varepsilon)$ (where T is used to define the eddy-viscosity and appears in the production and dissipation terms of the ε-equation). Abdon & Sundén [99] showed that the Durbin realizability condition improves Nusselt number predictions using a linear $k-\varepsilon$ model in impinging jet flows and Behnia *et al*. [100, 101] demonstrated that the elliptic-relaxation $\left(v^2-f\right)$ model incorporating the correction also performs well. In the NLEVM approach, contributions from the non-linear terms result in a better representation of the normal stresses and hence improve the stagnation-point behaviour. Differential stress models involve the solution of transport equations for the normal stresses which enables more elaborate methods of overcoming the stagnation-point problem to be employed (see [65]).

There have been a number of previous numerical simulations of impinging jet flows using wall functions. Heyerichs & Pollard [102] compared the performance of six low-Reynolds-number models and three wall functions in a 2-*D* impinging jet flow with $Re = 10,000$ and $H/D = 2.6$. No definitive conclusions about the superior performance of any one of the wall functions was made, except for the general comment that wall functions are unsuitable for complex flows where the assumptions used in their derivation are not valid. They also noted that the low-*Re* $k-\omega$ model gave slightly better predictions than the low-*Re* Launder-Sharma $k-\varepsilon$ model, although they also showed that the Yap correction had a negligible effect on the Nusselt number at the stagnation point. Amano & Brandt [103] studied a range of impinging jet nozzle-to-plate distances, ranging from 2 to 40 nozzle diameters, and Reynolds numbers from $50,000$ to $300,000$. They found that good agreement could be obtained between experimental and numerical predictions for the velocity, pressure and skin friction, using a linear $k-\varepsilon$ model with the Chieng & Launder wall function. Further papers by Amano & Jensen [104] and Amano & Sugiyama [105] showed that some small improvements could be made in predicting the stagnation-point heat transfer by solving transport equations for both k and ε in the

near-wall cell[3]. The results of these papers contrast with the more recent findings of Ashforth-Frost & Jambunathan [106] who found that for a confined impinging jet at a Reynolds number of $20,000$ and a nozzle-to-plate spacing of 2 jet diameters, the kinetic energy near the stagnation point was overpredicted by a factor of 9. They used the PHOENICS code with a linear $k-\varepsilon$ model and a wall function based on the velocity log-law and local-equilibrium assumptions. The poor performance of the numerical simulation in the stagnation region was attributed to both the isotropic linear eddy-viscosity model and the wall function. Bouainouche *et al*. [107] evaluated the performance of a simple wall function, based on the velocity log-law and prescribed nodal values for k and ε, and a "generalized" wall function in which a simplified transport equation for k was solved in the near-wall cell with cell-averaged production and dissipation rate source terms. Both approaches were shown to have shortcomings in the prediction of wall shear stress for impinging jet flows, although the latter model showed a lower sensitivity to changes in the near-wall grid spacing. A hybrid wall function was proposed which switched from the generalized wall function, used in the impingement zone, to the simple wall function, used downstream, at an *ad hoc* prescribed radial distance. Vieser *et al*. [108] studied a range of heat transfer problems with the CFX code using the $k-\varepsilon$, $k-\omega$ and SST turbulence models with wall functions. They found that good agreement between computational and experimental results could be obtained for $H/D=2$ and $Re=23,000$ using a linear $k-\varepsilon$ model with the scalable wall function (a reoptimized version of the wall-function proposed by Grotjans & Menter [47]).

In the present study, calculations are compared to the experimental heat transfer data of Baughn *et al*. [94] and the velocity and Reynolds stress data of Cooper *et al*. [95]. Jambunathan *et al*. [109] provide a comprehensive review of experimental heat transfer measurements for the impinging jet flow. The paper by Behnia *et al*. [101], which focuses mainly on the behaviour of the elliptic relaxation turbulence model in impinging flows, noted that there is considerable scatter in experimental measurements of the Nusselt number. They selected five recent sets of experimental Nusselt number data for $H/D=6$ and $Re=23,000$ and found differences of approximately 20-25%. These were attributed to differences in inlet conditions.

5.3 Computational Details

5.3.1 Models Used

Both the linear $k-\varepsilon$ and cubic non-linear $k-\varepsilon$ models presented in Chapter 2 were assessed in the impinging jet flow. For both models, results obtained using a low-Reynolds-number approach were compared to those obtained with four standard wall functions: Launder & Spalding (TEAM), simplified Chieng & Launder (SCL), Chieng & Launder (CL) and Johnson & Launder (JL), and with the new UMIST-*N* wall function. Some modifications to the expression for the cell-averaged

[3]Whereas in the Chieng & Launder approach, a transport equation is solved for k, but ε is specified at the near wall node from local-equilibrium assumptions.

production of turbulent kinetic energy, $\overline{P_k}$, used in the Chieng & Launder wall function, were also tested. The influence of the standard Yap correction and the differential length-scale correction were investigated with both models and two different c_μ functions were tested with the NLEVM. In the wall-function calculations, the sensitivity to changes in the size of the near-wall control volume were also assessed using different near-wall grid arrangements. In all of the results shown for the UMIST-*N* wall function, the same turbulence model was used in the subgrid as in the main-grid.

5.3.2 Numerical Methods

Calculations were made using the TEAM code discussed in Chapter 3. In all calculations, diffusion terms were approximated using central differencing, the QUICK scheme was used for the discretization of convection in the momentum and temperature equations and PLDS was used for k and ε. Near the entrainment boundary, QUICK was found to introduce some instability problems. PLDS was therefore used for all parameters (U, V, T, k and ε) in a region along the entrainment boundary extending roughly $0.5D$ into the flow domain. The dynamic and thermal fields are uncoupled in the impinging jet flow (i.e. the temperature field has negligible effect on fluid density) and therefore the thermal field was solved only once the dynamic field had converged. Typical under-relaxation factors for the main-grid code are shown in Table 5.1 and those for the subgrid solution in the UMIST-*N* wall function in Table 5.2.

U	V	P	k	ε	T	NL
0.35	0.35	0.5	0.45	0.45	0.60	0.4

Table 5.1: Under-relaxation factors used in the impinging jet flow with low-Reynolds-number models, standard wall-function calculations and in the main-grid with UMIST-*N* wall function calculations (*NL* refers to the Non-Linear EVM terms).

U	V	k	$\tilde{\varepsilon}$	NL
1.0	1.0	0.8	0.8	1.0

Table 5.2: Under-relaxation factors used for the subgrid transport equations with the UMIST-*N* wall function in the impinging jet flow.

Calculations involving the NLEVM with the UMIST-*N* wall function were started from an initially quiescent flow field using the linear $k-\varepsilon$ model and Yap correction across the subgrid domain and NLEVM with differential length-scale correction across the main-grid domain. After 500 iterations (approximately one third of the overall calculation time) the NLEVM and differential Yap correction were activated across the subgrid. Convergence was reached when the total non-dimensionalized residuals for the momentum and temperature equations were below 5×10^{-4} . It was confirmed that reducing residuals below this value had no effect on results. Calculations involving the differential Yap correction were, in general, less stable than those with the standard Yap correction and required greater under-relaxation in order to reduce residuals to the required limit. Greater under-relaxation

of the subgrid k and $\tilde{\varepsilon}$ was also required with the differential Yap correction as the near-wall cell size was increased. For the largest cell size ($DX = 500$) the under-relaxation factor for the subgrid k and $\tilde{\varepsilon}$ equations was $\alpha = 0.5$.

5.3.3 Domain and Grid

The flow domain for the impinging jet with a jet discharge height of 4 jet diameters was $4.5D$ in the wall-normal direction, which included $0.5D$ of inlet pipe length. A short length of pipe wall was included in the flow domain to reduce instability arising from the entrainment boundary near the jet inlet. In the radial direction, the domain extended 7 jet diameters.

The low-Reynolds-number grid, which used 90×70 (axial $\times$ radial) nodes, is shown in Figures 5.4 and 5.5. The y^+ values (calculated from $y^+ = c_\mu^{1/4} k^{1/2} y/\nu$) varied according to the turbulence model used, and are summarized in Table 5.3.

Turbulence Model	max. y^+at 5th node from the wall	max. y^+at 10th node from the wall
Linear $k-\varepsilon$	3	13
NLEVM	5	17

Table 5.3: y^+ values for the 90×70 low-Reynolds-number grid

A grid-dependence study was performed with a refined 120×90 grid (see Figure 5.6). This corresponded to an increase in the number of grid nodes of 70%, although the flow domain was also increased from 7 to 10 jet diameters in the wall-parallel direction. A small difference of 2% in the Nusselt number, limited to the region near the stagnation point ($r/D < 0.3$), was observed with the linear $k-\varepsilon$ model (see Figure 5.7). In the refined grid the first 10 cells were within $y^+ \leq 3$.

The high-Reynolds-number grids used with wall functions consisted of 45×70 (axial $\times$ radial) nodes, see Figures 5.8 and 5.9, and used an identical distribution of nodes in the radial direction to the low-*Re* grid. Four different near-wall cell widths were tested, denoted by $DX = 250, 300, 400, 500$, where the low-*Re*-grid near-wall cell width was $DX \approx 1$ (i.e. the near-wall cell size used by the wall functions was between 250 and 500 times larger than that used by the low-*Re* model). The quantity, DX, represents the physical thickness of the wall-adjacent cell in the wall-normal direction. The smallest width ($DX = 250$) corresponds to the lowest recommended size for wall functions based on logarithmic velocity profiles, i.e. $y^+ \geq 30$, and the largest cell ($DX = 500$) had a maximum y^+ of just over 300. The grid specification outside the near-wall cell was unchanged whilst the near-wall cell width was varied. The grid spacing for $DX = 250$ was continuous and so for $DX = 500$ there was a jump in cell size of $2:1$ from the near-wall cell to the adjoining cell (see the right-hand picture in Figure 5.10). The discontinuity in cell size for the large near-wall cells was a consequence of examining the effect of changing one variable only (the near-wall cell size) and not the effect of refining the overall grid. However, steps in cell size can lead to numerical inaccuracies and slow

convergence, particularly with more sophisticated turbulence models (such as the NLEVM tested here). If a continuous grid spacing is used for the largest near-wall cell size, i.e. 1:1 instead of 2:1 grid size ratios, the total number of grid nodes can be reduced from 45 to 41, convergence is improved and results are almost identical using the UMIST-*N* wall function (see Figure 5.11).

5.3.4 Boundary Conditions

Figure 5.1 shows a schematic of the boundary conditions employed in the impinging jet flow.

Inlet Pipe Flow

The inlet conditions at the jet discharge were specified using a fully developed pipe flow with Reynolds number, $Re = 70,000$ (based on bulk inlet velocity, jet diameter and the fluid properties of air at room temperature, $\mu = 1.82 \times 10^{-5} kg/m/s$ and $\sigma = 0.71$). The pipe flow was calculated separately using a parabolic solver (as in Suga [34]). In terms of coding the inlet conditions into TEAM; the velocities, turbulence scalars (k, ε and μ_t) and temperature were simply specified at the domain boundary nodes.

Axis of Symmetry

Along the axis of symmetry, zero-gradient conditions were applied for axial velocity components, turbulence scalars and temperature. To implement zero-gradient conditions in the main-grid, the nodal value on the boundary of the domain was set equal to the neighbouring nodal value (inside the domain) and the flux term associated with the boundary was set to zero in the discretized transport equation (i.e. $a_W = 0$ for the symmetry axis on the west cell face, shown in Figure 5.1). Similarly, in the subgrid, the values of V, k, $\tilde{\varepsilon}$ and T on the boundary were set equal to the neighbouring subgrid values. The radial velocity at the boundary nodes situated on the axis of symmetry was set to zero.

Entrainment

For the entrainment boundary condition at the northern edge of the flow domain, shown in Figure 5.1, different constraints were applied depending upon the local flow direction. If the fluid was entering the domain, Dirichlet conditions were applied: k and ε were given small but finite values ($k = V_N^2 \times 10^{-7}$, where V_N is the axial velocity through the entrainment boundary, and $\varepsilon = k$ so that $\mu_t = c_\mu k^2/\varepsilon = 0.09$), the radial velocity was set to zero and the temperature of the flow entering the domain was set to the ambient temperature. If fluid was leaving through the entrainment boundary, Neumann conditions were applied: values of U, k, ε or T on the boundary were set equal to the neighbouring nodal values just inside the domain and the flux coefficient through the boundary was set to zero ($a_N = 0$).

Irrespective of whether the flow was into or out of the domain, the axial velocity on the boundary of the domain, V_N, was set equal to the neighbouring nodal value and the pressure at the node just inside the entrainment boundary was set to zero.

Outlet

Although in theory the flow through the right-hand face of the domain shown in Figure 5.1 should be leaving the domain, during the iteration process flow may enter or leave through the boundary. For this reason the entrainment conditions described above were also used for the circumferential exit plane. The only difference here was that the radial U-velocity specified on the boundary was determined from:

$$\frac{\partial (rU)}{\partial r} = 0 \tag{5.3}$$

This condition was used to satisfy continuity within the cells adjacent to the exit plane.

Pipe Wall

It was necessary to include a short length of pipe at the jet inlet to improve stability. The surfaces of the pipe wall were treated with TEAM wall functions and the nodes inside the pipe wall had properties set to zero by the source conditions $s_U = 0$ and $s_P = -10^{30}$. The wall function treatment of the inlet pipe wall was not changed throughout the course of the calculations. Only the wall treatment applied to the impingement wall was varied.

Impingement Wall

Either a low-Reynolds-number model approach was used for the impingement wall or wall functions were applied. Heat transfer predictions were made assuming a constant heat flux from the wall surface. In the Nusselt number comparisons shown later, results from the calculations are compared to the experimental data of Baughn *et al*. [94]. In their experiments, Baughn *et al*. employed a transient technique[4] to obtain heat transfer measurements for constant wall temperature conditions. There is a degree of uncertainty in measuring transient phenomena. Baughn *et al*. performed an analysis of this and estimated the uncertainty to be less than 7%.

Figure 5.12 shows the predicted Nusselt number using constant heat flux (CHF) and constant wall temperature (CWT) conditions. The two calculations used the non-linear $k-\varepsilon$ model of Craft *et al*. [67] and the "standard" Yap correction. Prediction of the Nusselt number at the stagnation point was not affected by the choice of thermal boundary condition. However, the trough and peak in the predicted Nu downstream of the stagnation point occurred slightly closer to the jet axis with the CWT treatment than with CHF (CWT gave the min./max. inflexion points at $r/D \approx 1.05/1.65$, respectively, whereas CHF gave them at $r/D \approx 1.2/1.9$). In the radial-wall-jet region $r/D > 2.5$, CWT also gave a lower value of Nusselt number than CHF (a difference of up to 9%).

When using constant wall temperature conditions, there is greater heat transfer at the stagnation point than with constant heat flux boundary conditions. The fluid in the boundary layer adjacent

[4]The impingement plate, which was coated with a layer of liquid crystals, was heated to a set temperature in an oven. The plate was then covered with an insulating plate, taken out of the oven and placed in path of the impinging jet. Video recording equipment was activated, the insulating plate was removed and the coloured fringes on the liquid crystals were recorded.

to the wall in the CWT case is therefore at a higher temperature. Consequently, downstream from the impingement zone the temperature difference between the fluid and the wall is less and the heat transfer coefficient is lower with CWT than with CHF boundary conditions.

5.4 Calculated Flow Results

5.4.1 Linear $k-\varepsilon$

Low-Reynolds-Number Model

The linear $k-\varepsilon$ model is well known to overpredict the levels of turbulence energy, and hence heat transfer, at a stagnation point (see, for example, Craft *et al*. [65]). Profiles of the RMS velocity (Figure 5.13) show that the normal stress at the stagnation point is significantly over-predicted by the low-*Re* $k-\varepsilon$ model: the predicted peak wall-parallel u'-velocity is nearly three times the measured value whilst the wall-normal v'-velocity is approximately twice the size of the u'-component. The large predicted stress anisotropy at the stagnation point falls as one moves radially outwards to $r/D = 1$ and for $r/D \geq 1.5$ the u'- and v'-velocity components are practically identical. This behaviour in the shear flow region of the impinging flow is as would be expected from an isotropic linear model (where the normal stresses tend to $\overline{u_i^2} = 2k/3$ in the absence of any normal strain). Contrary to these predictions, the experimental data of Cooper *et al*. [95] shows the Reynolds stress remaining anisotropic at $r/D \geq 1.5$ with the streamwise (wall-parallel) component exceeding the wall-normal component $\left(v' \approx 2/3u'\right)$. Nusselt number predictions using the low-Reynolds-number $k-\varepsilon$ model (solid line in Figure 5.15) show that heat transfer at the stagnation point is overpredicted by more than 100% even with the Yap correction. The secondary peak in Nusselt number, observed in the experiments of Baughn *et al*. at $r/D \approx 2$, is also entirely missed.

Standard Wall Functions

Resultant velocity profiles are shown for the four standard wall functions: TEAM, SCL, CL, and JL in Figure 5.14. The four wall functions give practically identical results. Overall, the predicted velocity is in fair agreement with the experimental measurements although the near-wall peak in the predicted velocity is too low for $(0.5 \leq r/D \leq 2.5)$ and the velocity profile is too steep for $r/D \geq 1.5$. The poor performance of the wall functions is partly because the experimental maximum velocity occurs between the first nodal position and the wall. The near-wall cell size could not be reduced further without causing problems downstream, where the near-wall node would no longer occupy the log-law region and would fall inside the viscous sublayer[5]. It is impossible to draw conclusions from the velocity profiles about the relative performance of the different wall functions. This is true also of the Reynolds stress profiles (not shown). However, the Nusselt number predictions obtained using

[5]Such problems could be overcome if one used a non-orthogonal grid in which the near-wall cell size increased with distance from the axis of symmetry. This approach was not possible with the TEAM code, employed to study the impinging jet flow, which could only use a Cartesian grid arrangement.

the four standard wall functions are markedly different (Figures 5.15 – 5.18). In general, all of the standard wall functions are in poor agreement with the low-*Re* model predictions although they are in somewhat better agreement with the experimental results. The TEAM, CL and JL wall functions incorrectly predict the maximum heat transfer to occur at a distance of approximately $r/D \approx 0.5$, whilst the SCL wall function has a plateau between $r/D = 0$ and 0.5. All four wall functions predict the correct shape of the Nusselt number profile in the shear flow region $(r/D \geq 2.5)$ although there is significant discrepancy in the actual Nu levels in this region: the TEAM wall function results are lower than the experimental data points, the SCL and JL wall functions are higher and the CL wall function results are in good agreement with the experiments. None of the standard wall functions predict the secondary peak in Nu at $r/D = 2$, although this is due more to the turbulence model employed in the calculations. All of the standard wall functions show some sensitivity to the size of the near-wall cell. This sensitivity is greatest with the TEAM wall function, where a doubling of the cell size (from $DX = 250$ to 500) results in a drop in Nusselt number of approximately 10%. There are a number of features of the TEAM treatment which may be responsible for this behaviour, such as the assumed linear velocity profile used to calculate the strain-rate $(\partial U/\partial y)$ in the expression for average production (Equation 2.61) and the integration of P_k and ε across the whole near-wall cell (rather than just to the edge of the viscous sublayer). The least sensitivity to the cell size is shown by the CL wall function which calculates the wall shear stress using the value of k extrapolated to the edge of the viscous sublayer. Overall, the SCL wall function shows the behaviour closest to the low-*Re* model results of all the standard wall functions. Profiles of y^+ (which changes along the length of the wall) for the different near-wall sizes $(DX = 250, 300, 400, 500)$ are shown in Figure 5.19 using the CL wall function.

UMIST-*N* Wall Function

In comparison to the standard wall function results, the UMIST-*N* wall function shows good agreement with the low-*Re* model predictions of the Nusselt number (Figure 5.20). There is also practically no variation in predicted Nu due to changes in the size of the near-wall main-grid control volume (profiles of y^+ for the different near-wall cell sizes are shown in Figure 5.21). There is, however, a small discrepancy between UMIST-*N* and low-*Re* Nusselt number near the stagnation point ($r/D < 1$). At the stagnation point, the wall-normal velocity profiles across the subgrid are in good agreement with the corresponding low-Reynolds-number model profiles (see the earlier discussion in Section 4.3.1, in particular Figure 4.6). However, near-wall profiles of turbulent kinetic energy, k, (see Figure 5.22) show that the main-grid k values are lower than the low-*Re* model results outside the wall-function region. To investigate whether this discrepancy was due to an insufficient resolution of the peak in kinetic energy, which occurs in the main-grid region, the number of main-grid nodes normal to the wall was increased from 45 to 51, with clustering of nodes near the wall (Figure 5.23). This decreased the y^+ at the stagnation point from approximately 170 to 60 and improved the main-grid resolution of the kinetic energy peak (Figure 5.24). This improved the agreement between the Nusselt number

predicted by the UMIST-*N* wall function and the low-*Re* model (see Figure 5.25). This refinement of the near-wall grid was not applied in other tests since downstream from the stagnation point y^+ decreased to approximately 10, which is below the minimum value recommended in standard wall functions. The minimum size of the near-wall control volume is not restricted with the UMIST-*N* wall function since low-Reynolds-number model equations are solved in the main-grid and no assumed profiles are used across the near-wall cell.

To confirm that the underpredicted Nusselt number shown in Figure 5.20 was a consequence of inadequate main-grid resolution and not some effect introduced by decreasing the size of the subgrid region, the same near-wall cell size was used as in previous cases, with cell sizes in the range $DX = 250 \rightarrow 500$, but the adjoining main-grid cells were made 2.5 times smaller, see Figure 5.26. The predicted *k*-profiles using this grid arrangement and a near-wall cell size of $DX = 250$, shown in Figure 5.27, display a marked improvement in capturing the low-Reynolds-number *k*-profile compared to the earlier case where a coarse main-grid mesh was used. The UMIST-*N* wall function Nusselt number (Figure 5.28) is in good agreement with the result obtained when the main-grid was refined and the near-wall cell size was reduced to $y^+ \approx 60$ (compare to Figure 5.25). Although this test confirms that the original underprediction of the UMIST-*N* Nusselt number shown in Figure 5.20 was caused by insufficient near-wall main-grid resolution, this grid arrangement is not generally recommended, since the discontinuity in main-grid cell sizes, shown in Figure 5.26, may lead to inaccuracies in interpolating and determining gradients at the near-wall cell boundary[6] and will increase convergence times, particularly when more sophisticated turbulence models are applied. Interestingly, though, this same approach of using a relatively fine grid up to the near-wall cell was advocated by Goncalves & Houdeville [110] in their study of transonic flows over airfoils using wall functions. It also has some similarities to the approach of Grotjans & Menter [47] where the edge of the grid is treated as the outer limit of the viscous sublayer, rather than the wall, to enable unlimited grid refinement.

Log-Law Profiles

Profiles of the dimensionless velocity and temperature versus the wall distance, y^+, on semi-logarithmic axes are in Figures 5.29 and 5.30. The low-*Re* model distribution across the near-wall region is compared to the UMIST-*N* and Chieng & Launder wall functions and the "universal" log-law at 8 radial positions. The CL wall function line intercepts the universal log-law line, since the log-law is used to prescribe the velocity and temperature at the near-wall node. It is immediately obvious from these plots that the low-*Re* profiles do not match the law of the wall for velocity or temperature in the stagnation region $(0 < r/D < 1)$. This helps to explain why profiles of the Nusselt number predicted by the standard wall functions are so different from those obtained using low-*Re* model treatments in the vicinity of the stagnation point. Further downstream, $r/D > 1.5$, the velocity log-law is in surprisingly good agreement with the low-*Re* profile. However, the slope of the low-*Re* T^+ profile is

[6] since the gradient defined using central differencing between values at two nodes is more likely to reflect the gradient midway between the two nodes than the gradient in close proximity to one of the nodes.

steeper than the temperature log-law so that the temperature log-law is only valid for a narrow band of $40 < y^+ < 70$.

The UMIST-*N* wall function profiles of U^+ and T^+ are in excellent agreement with the low-*Re* profiles across the entire flow domain, despite the relatively coarse main-grid used in the wall function calculations. In both velocity and temperature plots, the subgrid profile matches that of the low-*Re* model almost exactly. Careful examination of the profiles shows that the subgrid profile does not intersect with the line joining the two near-wall main-grid nodes. This is due to the graph axes being logarithmic whilst a linear interpolation is used for the subgrid velocity and temperature boundary conditions.

Yap Correction

Figure 5.31 compares the performance of the standard and differential Yap corrections (given by Equations 2.16 and 2.17) with the low-*Re* linear $k-\varepsilon$ model. Clearly, either the standard or the differential correction improves significantly upon the heat transfer predictions of the linear $k-\varepsilon$ model without any length-scale correction. The Nusselt number predictions are notably lower overall and closer to the experimental values with the differential Yap correction than with the standard Yap correction. Figure 5.32 shows that the Yap correction has a much smaller influence on the heat transfer predictions when a standard wall function approach is employed than when a low-*Re* model is used. This behaviour is to be expected since standard wall functions fix the turbulence length scale at the near-wall node by specifying ε_P (Equation 2.51) and therefore in effect the Yap correction is not used in the near-wall row of cells[7]. The performance of the UMIST-*N* wall function with the differential Yap correction (Figure 5.33) shows a similar level of agreement with the low-*Re* model to that previously discussed for the standard Yap correction.

5.4.2 NLEVM

Low-Reynolds-Number Model

The impinging jet was one of the flows considered by Suga [34] in developing the non-linear $k-\varepsilon$ model[8] and more recent calculations by Craft *et al.* [67] have confirmed that the model performs well in this flow. Contour plots of the turbulent kinetic energy (Figure 5.34) show that the NLEVM predicts lower values of k at the stagnation point than the linear $k-\varepsilon$ model. Profiles of the RMS axial and radial velocity components in Figure 5.35 also show that the overall level of the predicted normal stress in the vicinity of the stagnation point is much lower and in far better agreement with the experimental measurements than that observed with the linear model (compare to Figure 5.13). At $r/D = 0.5$, the non-linear model correctly predicts the axial stress to be slightly larger than the

[7] The influence of the Yap correction on the predicted Nusselt number when standard wall functions are used is consequently dependent upon the thickness of the wall function region, i.e. the near-wall grid arrangement.

[8] Suga calibrated the model with respect to axisymmetric impinging jet flows with jet heights of $H/D = 2$ and 6, whereas the present study examines a jet height of $H/D = 4$.

radial stress and also the reverse trend at greater radii. However, the degree of anisotropy is slightly overpredicted for $1.0 \leq r/D \leq 1.5$ and underpredicted for $r/D \geq 2$. Craft *et al.* [30] acknowledged that the NLEVM underpredicts the stress anisotropy in plane channel flows but suggested that the correct normal stress behaviour is not a serious problem since it is the shear stress which controls the mean-flow behaviour in such flows, and this is well predicted. Figure 5.36 shows profiles of the shear stress for the impinging jet flow, and these are for the most part predicted accurately, although there is a significant overprediction of the shear stress magnitude at $r/D = 2$.

Nusselt number results for the low-*Re* NLEVM are shown as the solid line in Figure 5.37. The non-linear model predictions are in far better agreement with the experimental measurements than the linear model results shown, for example, in Figure 5.15. The overall shape of the experimental Nu profile is well matched with the secondary peak appearing at the correct location $(r/D = 2)$. However, the level of the predicted Nu is consistently around 10% higher than the experimental value.

Standard Wall Functions

Nusselt number predictions using the four standard wall functions are presented in Figures 5.37 to 5.40. All of the standard wall functions incorrectly predict the maximum heat transfer to occur downstream from the stagnation point, in the range $1 < r/D < 2$, with the TEAM wall function underpredicting the stagnation-point Nusselt number by 50%. All of the standard wall functions also display some sensitivity to the size of the near-wall control volume. Of the four standard wall functions, the Chieng & Launder wall function predicts the best overall shape of the Nusselt number.

Figure 5.42 shows the effect on the predicted Nusselt number of neglecting the normal stress contribution to the cell-averaged production $\overline{P_k}$ in the Chieng & Launder wall function (see discussion in Section 2.4). The stagnation point heat transfer is reduced by 30% compared to the case where normal stress contributions are included and agreement with the experimental data is considerably poorer. Figure 5.43 shows results using the Chieng & Launder wall function which has been modified to calculate the cell-averaged production, $\overline{P_k}$, assuming a linear profile of both shear and normal stresses across the fully-turbulent region of the near-wall cell (in the CL wall function results previously shown in Figure 5.39, the shear stress is assumed to vary linearly and the normal stresses to remain constant). The differences between Figures 5.39 and 5.43 are slight. In a further modification to the CL wall function, discussed in Section 2.4.6, the cell-averaged production is calculated assuming that the Reynolds stresses vary according to their wall-limiting behaviour across the viscous sublayer. This modification introduces a greater sensitivity to the size of the near-wall control volume (Figure 5.44), indicating that the assumed sublayer profiles of the Reynolds stresses are inappropriate.

When using standard wall functions, the strain-rate at the near-wall node $(\partial U/\partial y)_P$ can be calculated by differentiating the log-law, as discussed in Section 2.4.7. This strain-rate is used by the NLEVM to find the value of the strain-dependent c_μ function and the non-linear stress components within the near-wall cell. In fact, since the wall function replaces the production term in the near-wall cell with a cell-averaged value, $\overline{P_k}$, and since the diffusion to the wall is replaced by the wall

shear stress, τ_{wall}, the use of a modified $\partial U/\partial y$ only significantly influences diffusion of momentum through the face of the cell opposite the wall (the north face in Figure 2.1). Figure 5.45 shows the Nusselt number predictions for the impinging jet using the Chieng & Launder wall function with the log-law definition of $\partial U/\partial y$. The use of what could be considered as a more accurate representation of the strain-rate in fact leads to a worsening of the predicted Nusselt number, the log-law $\partial U/\partial y$ predicting entirely the wrong shape of the Nu profile near the stagnation point.

UMIST-*N* Wall Function

In contrast to the standard wall functions, the UMIST-*N* wall function with the NLEVM (Figure 5.46) shows excellent agreement with the low-*Re* model predictions. The wall function and low-*Re* results are practically indistinguishable for $r/D < 1.5$ and $r/D > 3$, with a maximum discrepancy of 8% at $r/D = 2$. The UMIST-*N* results also show negligible sensitivity to changes in the size of the near-wall control volume, whilst the Chieng & Launder wall function showed differences of up to 14% with the NLEVM.

Figure 5.47 shows a similar plot of the Nusselt number predicted by the UMIST-*N* wall function versus the low-*Re* NLEVM model predictions but now using the original c_μ function proposed by Craft *et al*. (Equation 2.33) – the previous results in Figure 5.46 were with the more recent c_μ function of Craft *et al.* [67] (Equation 2.36). The differences between the two c_μ functions are relatively minor. Using Equation (2.33) reduces the secondary peak in the Nu profile by approximately 5% bringing the predicted profile marginally closer to the experimental data. The UMIST-*N* wall function behaves similarly with either c_μ function.

Log-Law Profiles

Figures 5.48 and 5.49 compare the UMIST-*N* and Chieng & Launder wall function predictions of the velocity and temperature with the low-*Re* model predictions and "universal" law of the wall. The dimensionless velocity and temperature predicted by the low-*Re* model in the vicinity of the stagnation point are much lower than those predicted by the universal log-law. The Chieng & Launder wall function is tied to the log-law and consequently is in poor agreement with the low-*Re* profiles, whereas the UMIST-*N* wall function shows good agreement with the low-*Re* profiles across the whole flow domain. The slope of both the low-*Re* velocity and temperature profiles in the fully-turbulent region is somewhat steeper than that predicted by the log-law, even at $r/D = 3.5$, suggesting that agreement between log-law based wall functions and low-*Re* model calculations is only possible for a narrow range of near-wall cell sizes.

Yap Correction

Figure 5.50 compares the predicted Nusselt number using the low-*Re* NLEVM without the Yap correction, with the standard Yap correction (Equation 2.16) and with the differential Yap correction

(Equation 2.17). The purpose of the Yap correction is to suppress turbulence near a stagnation point. It seems therefore remarkable that when the Yap correction is removed, the Nusselt number is *reduced*. This behaviour is contrary to that observed previously with the linear $k-\varepsilon$ model (Figure 5.31).

The causes of this behaviour can be understood by examining the NLEVM expression for the Reynolds stress (Equation 2.27). Along the axis of symmetry, the vorticity tensor, Ω_{ij}, is zero and the expression for the Reynolds stress simplifies to:

$$\begin{aligned} \overline{u_i u_j} - \frac{2}{3}\delta_{ij}k &= \underbrace{-\nu_t S_{ij}}_{linear} \\ &\quad \underbrace{-0.1\nu_t \frac{k}{\tilde{\varepsilon}}\left(S_{ik}S_{kj} - \frac{1}{3}S_{kl}S_{kl}\delta_{ij}\right)}_{quadratic} \\ &\quad \underbrace{-5c_\mu^2\nu_t\left(\frac{k}{\tilde{\varepsilon}}\right)^2 S_{ij}S_{kl}S_{kl}}_{cubic} \end{aligned} \tag{5.4}$$

Assuming the ratio of $(k/\tilde{\varepsilon})$ to be large near the stagnation point, the c_μ function given by Equation (2.36) is approximately proportional to the ratio of $(\tilde{\varepsilon}/k)$:

$$c_\mu \propto \frac{\tilde{\varepsilon}}{k} \tag{5.5}$$

If one also assumes that the strain-rates are approximately equal whether the Yap correction is employed or not, then the cubic non-linear term in Equation (5.4) can be shown to vary in proportion to the eddy-viscosity. The quadratic term, on the other hand, is a function of the eddy-viscosity and the ratio of $(k/\tilde{\varepsilon})$. When the Yap correction is introduced, the turbulent length scale and hence the ratio of $(k/\tilde{\varepsilon})$ are decreased. This then decreases the quadratic term in Equation (5.4) which has the effect of increasing the wall-normal Reynolds stress, $\overline{v^2}$, and hence the production of k. It was found, although results are not shown here, that by making the quadratic coefficient c_1 in the NLEVM a linear function of c_μ, the dependence on $(k/\tilde{\varepsilon})$ is reduced and the NLEVM responds as anticipated to the Yap correction, i.e. heat transfer rates are reduced when the Yap correction is activated.

The difference between the standard and differential Yap correction results are less significant with the NLEVM than those shown previously for the linear model. The differential correction reduces the Nusselt number at the stagnation-point (by around 8% compared to the standard correction) and further downstream $(r/D > 1)$. Results are therefore in marginally better agreement with the experimental data using the differential length-scale correction.

5.5 Computational Costs

Tables 5.4 and 5.5 compare the computing times for the Chieng & Launder wall function, the UMIST-*N* wall function, and low-Reynolds-number treatments for the linear and non-linear $k-\varepsilon$ models. Both wall functions use identical main-grids and the low-Reynolds-number grids only involve refinement normal to the wall (the grid in the radial direction is identical in wall function and low-*Re* model simulations). Main-grid under-relaxation factors are identical for all computations and subgrid under-relaxation factors are those presented in Table 5.2. Calculations were performed on a Silicon Graphics O_2 with the same levels of compiler optimization in each case.

Model Tested	No. of Nodes (axial×radial)	Time per Iter (*s*)	No. of Iterations	Total CPU Time (*s*)	Relative CPU Time
Chieng & Launder WF	45×70	0.147	1523	224	1
UMIST-*N* WF	$(45+[40])\times 70$	0.228	1392	318	1.42
Low-*Re*	90×70	0.270	9698	2616	11.68

Table 5.4: Computing times for the impinging jet flow using the linear $k-\varepsilon$ model

Model Tested	No. of Nodes (axial×radial)	Time per Iter (*s*)	No. of Iterations	Total CPU Time (*s*)	Relative CPU Time
Chieng & Launder WF	45×70	0.158	1426	226	1
UMIST-*N* WF, option 1	$(45+[40])\times 70$	0.224	1392	313	1.38
UMIST-*N* WF, option 2	$(45+[40])\times 70$	0.260	1380	359	1.59
UMIST-*N* WF, option 3	$(41+[45])\times 70$	0.253	1568	398	1.76
Low-*Re*, option 1	90×70	0.318	9346	2971	13.14
Low-*Re*, option 2	90×70	0.324	9116	2955	13.08

Table 5.5: Computing times for the impinging jet flow using the non-linear $k-\varepsilon$ model

All the calculations reported in Table 5.4 employed the "standard" Yap correction. The Chieng & Launder wall function results given in Table 5.5 employed the Craft *et al*. [30] model and "standard" Yap correction. The following options are shown for the subgrid wall function:

1. Craft *et al*. [67] model with "standard" Yap correction and small near-wall cell size ($DX = 250$)
2. Craft *et al*. [67] model with differential Yap correction and small near-wall cell size ($DX = 250$)
3. Craft *et al*. [67] model with differential Yap correction and large near-wall cell size ($DX = 500$)

The large near-wall cell ($DX = 500$) corresponds to a doubling in the size of the smaller ($DX = 250$) near-wall cell. The two cell sizes represent the extremes of recommended near-wall cell sizes for log-law based wall functions: for the small ($DX = 250$) cell the minimum y^+ was around 30 and in the large ($DX = 500$) cell the maximum y^+ was around 300. Two options are shown for the low-Reynolds-number calculations as follows:

1. Craft *et al*. [30] model with "standard" Yap correction
2. Craft *et al*. [67] model with differential Yap correction

5.6 Discussion & Conclusions

The principal aim of examining the impinging jet flow was to assess whether the UMIST-*N* wall function could obtain good agreement with low-Reynolds-number model predictions in a flow far from local equilibrium. Using both linear and non-linear models it has been shown that UMIST-*N* does indeed produce very nearly the same results as with the corresponding low-*Re* model. When used with the linear $k-\varepsilon$ model, the UMIST-*N* wall function slightly underpredicts the low-*Re* model Nusselt number results near the stagnation point. This was shown to be mainly due to insufficient resolution of the peak turbulent kinetic energy in the main-grid. Refinement of the main-grid improved resolution of this peak and consequently improved the Nusselt number prediction, whilst demonstrating that the UMIST-*N* wall-function can be applied in regions where y^+ falls to approximately 10 (below that recommended for standard wall functions based on a log-law velocity profile). When used with the non-linear $k-\varepsilon$ model, there was excellent agreement between the UMIST-*N* wall function and low-*Re* model predictions. Tests with four log-law-based wall functions showed that their performance is poor near the stagnation point. Semi-logarithmic profiles of the dimensionless velocity and temperature (U^+ and T^+ versus y^+) indicated that the flow predicted by the low-*Re* NLEVM in the vicinity of the stagnation point does not follow the law-of-the-wall. The fact that the low-*Re* NLEVM shows good agreement with the experimental Reynolds stress and heat transfer results therefore indicates that wall functions which are based upon the log-law will be unlikely to predict impinging flows with accuracy. Standard log-law wall functions were also shown to be sensitive to the size of the near-wall control volume whereas the UMIST-*N* wall function showed practically no sensitivity. The new wall function leads to a modest increase in computing time of up to 60% compared to a standard wall function. This is, however, an order-of-magnitude less than a standard low-Reynolds-number treatment.

In addition to examining the performance of the new wall function, two different turbulence length-scale corrections were tested: the Yap correction [64], and the differential Yap correction of Craft *et al*. [67]. The latter correction removes the dependence upon the wall-normal distance, which can be difficult to define in flows with complex geometry. The differential Yap correction was shown to have a stronger influence on the turbulence length scale than the standard Yap correction and, with a linear $k-\varepsilon$ model, decreased the predicted Nusselt number at the stagnation point by nearly 25%. Its effect with the non-linear model was shown to be less significant.